Room-temperature spin-to-charge conversion in sputtered bismuth selenide thin films via spin pumping from yttrium iron garnet

Cite as: Appl. Phys. Lett. **114**, 102401 (2019); https://doi.org/10.1063/1.5054806 Submitted: 03 September 2018 . Accepted: 07 February 2019 . Published Online: 12 March 2019

Mahendra DC, Tao Liu, Jun-Yang Chen 🗓, Thomas Peterson, Protyush Sahu, Hongshi Li, Zhengyang Zhao 🗓, Mingzhong Wu, and Jian-Ping Wang







View Onlin

ARTICLES YOU MAY BE INTERESTED IN

Antiferromagnetic NiO thickness dependent sign of the spin Hall magnetoresistance in γ -Fe₂O₃/NiO/Pt epitaxial stacks

Applied Physics Letters 114, 102405 (2019); https://doi.org/10.1063/1.5080766

Conversion of spin current into charge current at room temperature: Inverse spin-Hall effect Applied Physics Letters 88, 182509 (2006); https://doi.org/10.1063/1.2199473

Spin valve effect induced by spin-orbit torque switching
Applied Physics Letters 114, 092404 (2019); https://doi.org/10.1063/1.5086775





Room-temperature spin-to-charge conversion in sputtered bismuth selenide thin films via spin pumping from yttrium iron garnet

Cite as: Appl. Phys. Lett. **114**, 102401 (2019); doi: 10.1063/1.5054806 Submitted: 3 September 2018 · Accepted: 7 February 2019 · Published Online: 12 March 2019







Mahendra DC,¹ Tao Liu,² Jun-Yang Chen,³ (b) Thomas Peterson,¹ Protyush Sahu,¹ Hongshi Li,⁴ Zhengyang Zhao,³ (b) Mingzhong Wu,² and Jian-Ping Wang^{1,3,4,a)}

AFFILIATIONS

- ¹School of Physics and Astronomy, University of Minnesota, Minneapolis, Minnesota 55455, USA
- ²Department of Physics, Colorado State University, Fort Collins, Colorado 80523, USA
- ³Department of Electrical and Computer Engineering, University of Minnesota, Minneapolis, Minnesota 55455, USA
- ⁴Department of Chemical Engineering and Materials Science, University of Minnesota, Minneapolis, Minnesota 55455, USA

ABSTRACT

We investigated spin-to-charge current conversion in sputtered $Y_3Fe_5O_{12}$ (YIG)/granular bismuth selenide (GBS) bi-layers at room temperature. The spin current is pumped to the GBS layer by the precession of magnetization at ferromagnetic resonance in the YIG layer. The spin-mixing conductance is determined to be as large as $(13.64 \pm 1.32) \times 10^{18}$ m⁻², which is larger than that of YIG/Pt and comparable or better than that of YIG/crystalline bismuth selenide indicating that GBS is a good spin-sink. The figure of merit of spin-to-charge conversion, the inverse Edelstein effect length ($\lambda_{\rm IEE}$), is estimated to be as large as (0.11 ± 0.03) nm. $\lambda_{\rm IEE}$ shows GBS film thickness dependence, and its value is three times as large as in crystalline bismuth selenide. The $\lambda_{\rm IEE}$ value larger than that of crystalline bismuth selenide and other topological insulators indicates that the spin-to-charge conversion is due to the spin-momentum locking. As the thickness of GBS increases, $\lambda_{\rm IEE}$ decreases, which means the figure-of-merit of spin-to-charge conversion is influenced by grain size.

Published under license by AIP Publishing. https://doi.org/10.1063/1.5054806

Spin-orbit coupling is an efficient mechanism for the generation and detection of spin current in spintronic devices. 1,2 The detection of spin current is possible through the inverse spin Hall effect (ISHE),^{3–8} the inverse Edelstein effect (IEE),^{9–} and the inverse Rashba-Edelstein effect (IREE);^{20–23} these effects have been realized in heavy metals, in topological insulators (TIs), and at certain interfaces such as Ag/Bi,²⁰ Ag/Sb,²¹ and lanthanum aluminate (LAO)/strontium titanate (STO),²² respectively. Spin-to-charge conversion can be used in logic devices such as the magneto-electric spin-orbit (MESO) device. 24,25 One can examine the spin-to-charge conversion via spin pumping; to obtain strong spin-pumping signals and avoid spurious effects on the spin-pumping signal, one usually uses the ferromagnetic resonance (FMR) in low-damping ferrimagnetic insulators such as yttrium iron garnets (YIG).7,3 ²⁹ So far, spin-momentum locking in crystalline TIs is the most efficient mechanism for the spin-to-charge conversion. 12,15 However, spin pumping from YIG to granular TIs has not been studied yet. In our previous report, we observed that the charge-to-spin conversion in sputtered granular bismuth selenide (GBS) films can be significantly influenced by quantum confinement (QC).³⁰

In this report, we present the study of spin pumping from YIG films to sputtered GBS films at room-temperature. The spin-mixing conductance $(g_{\uparrow\downarrow})$ is determined to be as large as $(13.64\pm1.32)\times10^{18}~{\rm m}^{-2},$ which is larger than that of YIG/Pt and YIG/Bi₂Se₃ 13 indicating that GBS is a good spin-sink. Furthermore, $g_{\uparrow\downarrow}$ as a function of GBS film thickness does not show any particular behavior, and it agrees with previous reports on crystalline Bi₂Se₃ (CBS). $^{13.31}$ $g_{\uparrow\downarrow}$ should increase as the thickness of the spin-sink increases if the spin-to-charge conversion is only due to ISHE. $^{31-33}$ The figure of merit of the spin-to-charge conversion, the inverse Edelstein effect length $(\lambda_{\rm IEE})$, is estimated to be as large as (0.11 \pm 0.03) nm. This efficient spin-to-charge conversion is due to the combination of the conventional spin-momentum locking and the QC-produced additional spin-momentum locking contribution. 30

^{a)}Author to whom correspondence should be addressed: jpwang@umn.edu.

We prepared Gd₃Ga₅O₁₂ (GGG)/YIG (20 nm)/GBS (4 nm)/ MgO (2 nm)/Ta (2 nm) and (GGG)/YIG (30 nm)/GBS (8, 12, and 16 nm)/MgO (2 nm)/Ta (2 nm) samples for the spin-pumping measurements. Unless otherwise stated, we label samples with 4, 8, 12, and 16 nm thick GBS films as GBS4, GBS8, GBS12, and GBS16 samples, respectively. A reference sample GGG/YIG (20 nm)/Pt (5 nm)/MgO (2 nm)/Ta (2 nm) was also prepared and was labelled as the Pt sample. The YIG films were grown on GGG (111) wafers by RF magnetron sputtering at room temperature first and then in-situ annealed at 800 °C for 2h under the oxygen pressure of 1Torr. For the annealing process, the heating rate was 10 °C/min, while the cooling rate was 2 °C/min. GBS thin films were grown on GGG/YIG (20 nm and 30 nm) films at room temperature by sputtering a composite Bi₂Se₃ target with a base pressure of 5.0×10^{-8} Torr. The concentration of Bi and Se in GBS films is determined to be 43% and 57%, respectively, using X-ray photoelectron spectroscopy. The thin films were patterned into rectangular strips with the width and the length being 620 μ m and 1500 μ m, respectively, using optical lithography and ion milling. Then, 50 nm thick SiO₂ was deposited using sputtering to insulate the films from waveguides. In the last step of lithography, contacts and co-planar waveguides were defined. A 10 nm thick Ti layer followed by 150 nm thick gold layer was deposited using an e-beam evaporator for electrical contacts and waveguides. The spin-pumping measurements were performed on a co-planar waveguide that had a signal line width of 75 μ m, a ground width of 225 μ m, and a ground-to-signal line separation of $37.5 \,\mu\text{m}$.

Figures 1(a) and 1(c) present an atomic force microscopy (AFM) image of the YIG (20 nm) film grown on the GGG substrate and an AFM image of a GBS (8 nm) film grown on a thermally oxidized silicon substrate, respectively. The AFM characterization

FIG. 1. Characterization of YIG and GBS films. (a) and (c) AFM surface images of GGG/YIG (20 nm) and Si/SiO $_2$ /MgO (2 nm)/GBS (8 nm) samples, respectively. (b) FMR profile of the GGG/YIG (20 nm) sample. (d) TEM cross-sectional image of a YIG/BS sample.

of the YIG film shows that the film is smooth and has a rootmean-square (RMS) surface roughness of 0.11 ± 0.01 nm, while the AFM measurement of the GBS (8 nm) film shows that the film is granular, with a RMS roughness value of about 0.54 nm. The magnetic properties of the YIG film were characterized by FMR under an in-plane external magnetic field. The FMR line shape of the GGG/YIG (20 nm) film is presented in Fig. 1(b). Lorentzian trial functions were used to fit the FMR profiles to extract the FMR field and linewidth values. The excitation frequency versus the FMR field was plotted to determine the saturation magnetization using the Kittel formula, $f = \frac{\gamma}{2\pi} \sqrt{H_0(H_0 + 4\pi M_{eff})}$, where γ is the absolute gyromagnetic ratio, H_0 is the FMR field, and M_{eff} is the effective saturation magnetization. The FMR linewidth vs. frequency data were linearly fitted to estimate the Gilbert damping constant (α). M_{eff} and α were determined to be 139.54 \pm 0.24 emu/cc and (1.16 \pm 0.14) \times 10 $^{-4},$ respectively, for the GGG/YIG (20 nm) film. These values of $M_{\mbox{\scriptsize eff}}$ and α are comparable to previous reports. 34,35 The high-angle annular dark-field transmission electron microscopy (HAADF-TEM) image of the full stack structure used for the spin-pumping measurements is presented in Fig. 1(d). The microstructure shows that GBS and YIG are polycrystalline. The resistivity of GBS increases with the decrease in the temperature [supplementary material Fig. 1(a)]. The carrier concentration estimated from the Hall measurement was 2.85×10^{21} /cm³, with the electrons being the majority carriers in

The schematics of spin pumping from the YIG layer to the GBS layer is shown in Fig. 2(a). The RF field drives the magnetization of the YIG into precession at a fixed frequency in the GHz range. At resonance, the YIG layer pumps spins to the GBS layer and the spin-momentum locking in the GBS layer creates non-equilibrium charge accumulation. ^{18,19} The open circuit voltage

the GBS (8 nm) film [supplementary material Fig. 1(b)].

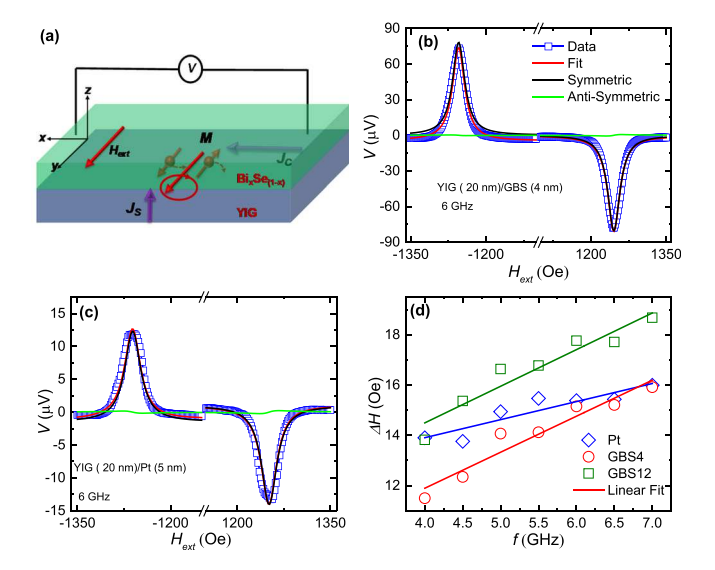


FIG. 2. Spin-to-charge conversion by sputtered GBS thin films. (a) Schematic of spin-to-charge conversion. (b) and (c) The spin-pumping voltage measured in GBS and reference Pt samples at an excitation frequency of 6 GHz. (d) The line-width as a function of excitation frequency.

build up can be measured by using a voltmeter. Figure 2(b) shows the measured open-circuit voltage (V) of the GBS4 sample as a function of the external magnetic field ($H_{\rm ext}$) at an excitation frequency (f) of 6 GHz and an excitation amplitude of 1.5 V (\sim 16.53 dBm). Moreover, V as a function of $H_{\rm ext}$ presented in Fig. 2(b) clearly shows sign reversal as $H_{\rm ext}$ changes the sign. This confirms that the V originates from spin-to-charge conversion due to some physical mechanism not the artifacts. V in the YIG/GBS spin-pumping is free from the anisotropic magnetoresistance (AMR) as YIG is an insulating ferrimagnet. The V experimental data are fitted to the symmetric and antisymmetric Lorentzians provided in the following equation:

$$V = \frac{V_{S}\Delta H^{2}}{\Delta H^{2} + \left(H_{ext} - H_{0}\right)^{2}} + \frac{V_{A}(H_{ext} - H_{0})}{\Delta H(\Delta H^{2} + \left(H_{ext} - H_{0}\right)^{2})}, \qquad \text{(1)}$$

where ΔH is the line-width. V_S is the coefficient of the symmetric component, while V_A is the coefficient of the anti-symmetric component. Negligibly, small VA is present in both BS and Pt samples. Since V_S flips sign when H_{ext} switches the direction, this component consists of the spin-to-charge voltage due to IEE $(V_{IEE})^{10,12,17,36,37}$ or ISHE. ^{3,5,38} However, one needs to be careful while referring V_S directly to the IEE or ISHE effects because the inductive coupling between the waveguide and the film could generate V_S. 36,39 In our case, if there is proximity-induced magnetization, it could mix with inductive coupling induced current, which could contribute to V_S. We confirmed that there is no proximity-induced magnetism in between YIG and GBS by performing anomalous Hall effect and out-of-plane AMR measurements. Additionally, the Seebeck voltage $(V_{SE})^{10,17}$ is attributed to the microwave heating, which is mixed with the V_{IEE} in V_S . V_{SE} has a symmetric line-shape but it does not change sign as Hext changes sign. We can simply separate VIEE and VSE using $V_{IEE} = (V_S(+H_0) - V_S(-H_0))/2$ and $V_{SE} = (V_S(+H_0) + V_S(-H_0))/2$ 2 relations. Figure 2(c) shows V as a function of H_{ext} at a constant excitation amplitude (1.5 V) for the Pt sample. As expected from the ISHE, V flips the sign when the Hext sign is flipped in the Pt sample.⁵ ΔH as a function of f is presented in Fig. 2(d). An increase in V as f decreases is consistent with the previous reports. ^{13,40} The damping constant (α) is obtained by using $\Delta H = \Delta_0 + \frac{4\pi}{\sqrt{3}2}\alpha f$ to fit the ΔH versus f data, where Δ_0 corresponds to the contribution of spatial inhomogeneity present in the YIG film. The α values for the GBS4, GBS8, GBS12, GBS16, and Pt samples are (3.5 ± 0.43) , (3.5 ± 0.46) , (2.40 ± 0.50) , (4.10 ± 0.49) , and $(1.7\pm0.33)\times10^{-3}$, respectively. Furthermore, the enhancement of α of the GBS samples as compared to the GGG/YIG value of $\alpha\sim(1.16\pm0.14)\times10^{-4}$ also corresponds to the spin-to-charge conversion. ⁴¹ Moreover, α enhancement can be due to spin-pumping, ^{33,41} spin-memory loss, ^{8,32,42,43} and interfacial spin-to-charge conversion. ²⁰ Further investigation is required to identify contribution of interfacial spin-to-charge conversion such as IREE.

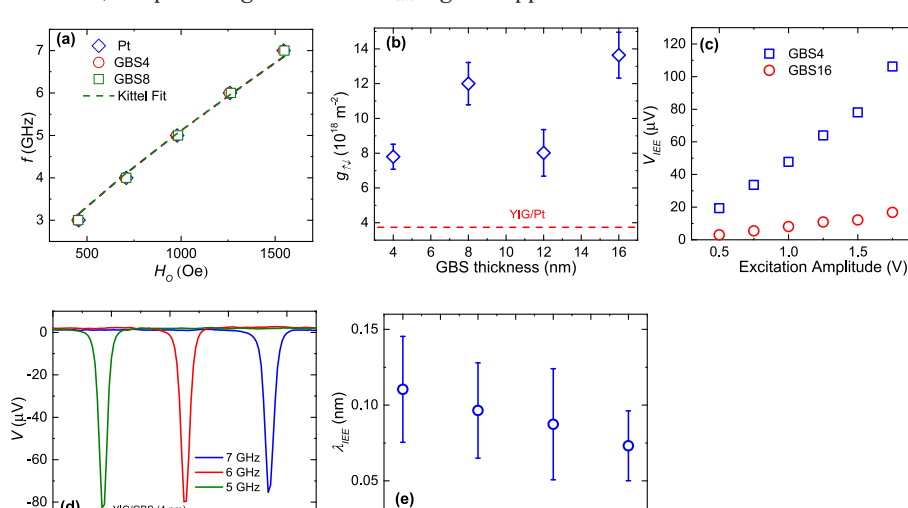
Figure 3(a) shows f as a function of H_0 . The fit corresponds to the Kittel formula. M_{eff} is estimated to be (185.42 \pm 7.42), (187.01 \pm 8.28), (185.42 \pm 8.71), (183.03 \pm 8.02), and (183.83 \pm 9.14) emu/cc for GBS4, GBS8, GBS12, GBS16, and Pt samples, respectively. Figure 3(c) shows $V_{\rm IEE}$ as a function of the excitation amplitude of the GBS4 and GBS16 samples. $V_{\rm IEE}$ as a function of the excitation amplitude is in agreement with our previous reports. 6,12 V as a function of $H_{\rm ext}$ at different f values is presented in Fig. 3(d). As is expected, V increases with a decrease in f.

The spin current density (J_s) injected from the YIG to the GBS layer is given by^{4,5}

$$J_{S} = \frac{g_{\uparrow\downarrow}\gamma^{2}h_{rf}^{2}\hbar}{8\pi\alpha^{2}} \frac{\left(4\pi M_{S}\gamma + \sqrt{\left(4\pi M_{S}\gamma\right)^{2} + 4\omega^{2}}\right)}{\left(4\pi M_{S}\gamma\right)^{2} + 4\omega^{2}} \frac{2e}{\hbar}, \qquad (2)$$

where M_S , $\omega(2\pi f)$, $h_{\tau f}$, $g_{\uparrow\downarrow}$, \hbar , and e are the saturation magnetization of YIG, the excitation frequency, the microwave RF field, Planck's constant, and the electronic charge, respectively. The spin-mixing conductivity is given by

$$\operatorname{Re}(g_{\uparrow\downarrow}) = \frac{4\pi M_{\rm s} t_{\rm FMI}}{g\mu_{\rm B}} (\alpha - \alpha_{\rm int}), \tag{3}$$



8 10 12 1 GBS thickness (nm)

FIG. 3. Characterization of spin-to-charge conversion (a) Excitation frequency as a function of resonance field fits according to the Kittel formula. (b) Spin-mixing conductance of GBS samples as a function of GBS film thickness. (c) Spin-to-charge conversion voltage as a function of the excitation amplitude. (d) Spin-pumping voltage as a function of requency. (e) IEE length as a function of the GBS film thickness shows thickness dependence.

1400

1600

⁰ (d) 800

1000

1200

H_{ext} (Oe)

where g, μ_B , t_{FMI} , and α_{int} are Landé's g-factor, the Bohr magneton, the YIG thickness, and the intrinsic value of the YIG damping constant, respectively. $g_{\uparrow\downarrow}$ for GBS samples obtained by using Eq. (3) is presented in Fig. 3(b). $g_{\uparrow\downarrow}$ for GBS samples is more than three times larger than that of the Pt sample. In addition, $g_{\uparrow\downarrow}$ values obtained in our GBS samples are better or comparable to the previously reported values in YIG/CBS¹³ (\sim 8 × 10¹⁸ m⁻²) and YIG/CBS³¹ (\sim 2.2 × 10¹⁹ m⁻²), which means that sputtered GBS is a good spin-sink.

At an excitation frequency of 6 GHz and an excitation amplitude of 1.5 V, J_s injected into the GBS4, GBS8, GBS12, GBS16, and Pt samples is 2.63, 3.89, 4.41, 3.34, and 5.12×10^5 A/m², respectively. These values of J_s are estimated by using the spin Hall angle of Pt as 0.07 ± 0.01 and the spin-diffusion length of $3.4 \pm 0.4 \,\mathrm{nm}^8$ for the extraction of h_{rf} . h_{rf} for the samples with different conductivities can be different because h_{rf} could be shielded differently. The skin depth of Pt and GBS is 2.30×10^{-6} and 3.98×10^{-5} m, respectively, which are much larger than the film thickness; so, h_{rf} is the same for YIG/Pt and YIG/GBS samples given that the input power is same. Note that the value of the spin Hall angle of Pt 0.07 ± 0.01 is obtained by performing independent spin-torque ferromagnetic resonance on the Pt (5 nm)/NiFe (6 nm) sample. 44 This value of the spin Hall angle of Pt is comparable to the previous reports.^{7,8,44} The efficiency of the spin-to-charge conversion for the IEE is given by 18,20 $\lambda_{\rm IEE} = rac{J_{\rm C}}{J_{\rm s}} = rac{V_{\rm IEE}}{{
m R}wJ_{
m s}},$ where R and w are the resistance and the width of the device, respectively. V_{IEE} , R, and w for the GBS4 sample are 79.29 μ V, 4400 Ω , and 620 μ m, respectively. λ_{IEE} for the GBS4 sample is estimated to be (0.11 \pm 0.03) nm. This value of $\lambda_{\rm IEE}$ is more than three times larger than that reported for YIG/CBS (0.035 nm)¹³ and more than an order of magnitude than reported for YIG/Bi/Ag (0.01 nm). 26 $\lambda_{\rm IEE}$ as a function of GBS is presented in Fig. 3(e). The error bars in λ_{IEE} are determined by incorporating errors in h_{rf} , $g_{\uparrow\downarrow}$, and α . λ_{IEE} shows GBS thickness dependence, which is in agreement with the figure-of-merit of charge-to-spin conversion as a function of GBS thickness presented in our previous report.³⁰ Unlike the thickness dependence in the case of heavy metals, in GBS, λ_{IEE} is correlated with the size of grains present in the GBS films. It should be noted that as the thickness of the GBS increases, the grain size also increases as demonstrated by TEM.³⁰ In the case of CBS, λ_{IEE} first increases and it remained constant after certain thickness, whereas in GBS it has shown thickness dependence.¹³ We also estimated the momentum relaxation time (τ_m) in the surface states of the BS8 sample using the relation 15,19,20 $\lambda_{IEE}=\upsilon_{f}\tau_{m},$ where v_f is the Fermi velocity. v_f for GBS (8 nm) is estimated to be 3.38×10^6 m/s. Using a $\lambda_{\rm IEE}$ value of 0.96 nm of the GBS8 sample, τ_m is determined to be 2.84×10^{-16} S, which is an order of magnitude shorter compared to the previously reported values on TIs and Rashba interfaces 15,22,45 but comparable to that at the Cu/Bi⁴⁶ interface.

Shiomi et al. reported a $\lambda_{\rm IEE}$ value of 0.1 nm due to the IEE in bulk insulating Bi_{1.5}Sb_{0.5}Te_{1.7} at 15 K.¹⁰ Jamali et al. and Deorani et al. reported room temperature spin-to-charge conversion by CBS due to the ISHE and IEE.^{12,38} Jamali et al. performed magnetization precession cone angle measurements to confirm the contribution of ISHE in the spin-to-charge conversion by CBS

but did not separate contributions of each effects. Deorani et al. separated contributions from ISHE and IEE by assuming that the surface state thickness of the CBS is 3 nm. Wang et al. observed spin-to-charge conversion in YIG/CBS mainly due to the IEE, and the estimated value of λ_{IEE} is as large as 0.035 nm at room temperature. From these aforementioned reports on spin-to-charge conversion by CBS, one can observe that there is contribution from IEE and ISHE. In our YIG/GBS samples, there could be contributions from ISHE, IREE, and IEE. λ_{IEE} as a function of GBS film thickness shows different behavior compared to YIG/Bi₂Se₃.¹³ It also does not show any hyperbolic tangent thickness dependent behavior, which is a typical behavior in the heavy metals. If we consider the spin-memory loss same as in the Pt/Py bilayer system in YIG/GBS, the behavior of λ_{IEE} remains the same at a smaller thickness.⁴⁷ The damping enhancement due to spin-memory loss in Pt/Py was estimated to be as large as 63%. 47 Now, the question arises why sputtered GBS films have higher $\lambda_{\rm IEE}$ as compared to MBE grown CBS?^{13,38} As the thickness of the films reaches a nano-scale, electrons can move freely in two dimensions, but electronic motion is confined along the normal to the film plane. Confinement quantizes the wavefunction of the electron. Consequently, the electronic properties of the material change drastically. In the case of sputtered GBS, from the AFM and TEM images, we can clearly see grains of nano-meter scale. In these nano-sized grains, the electronic motion is confined along three dimensions. In our previous report, we performed numerical simulations to study the effect of the grain size effect on the charge-to-spin conversion and found that the charge-to-spin conversion is largely influenced by the grain size effect.³⁰ There are additional discrete bands present in the case of ~10 nm scale grains compared to triangular crystals present in MBE grown TI films. Note that in the case of crystalline TI films, confinement is only along the normal of the film plane. The additional discrete bands present in grains of GBS, due to QC, contribute to the spin-momentum locking. In the case of spin-to-charge conversion, λ_{IEE} shows GBS film thickness dependence and it has a larger value than that of the CBS film, which confirms that the spin-to-charge conversion in GBS films is also influenced by QC in the grains of GBS films.

We demonstrated an easier way of growing an efficient spin-to-charge current converter, which can be readily utilized for large scale production. For the application point of view, it is important to have a large spin-to-charge conversion voltage as well as a widely used growth technique. GBS is grown by a magnetron sputtering technique, and we observed more than five times large spin-to-charge voltage at room-temperature compared to Pt, which makes sputtered GBS a good choice for the practical applications in logic devices such as MESO. The $\lambda_{\rm IEE}$ value of sputtered GBS is three times as large as that of CBS and $g_{\uparrow\downarrow}$ follows similar behavior as in YIG/CBS. This indicates that the origin of high spin-to-charge conversion by sputtered GBS is due to the spin-momentum locking, and it is also influenced by QC.

See supplementary material for the carrier concentration, the temperature dependent resistivity, and the TEM microstructure.

We would like to thank Jason C. Meyers for TEM. This work was supported in part by ASCENT, one of the six centers in JUMP, a Semiconductor Research Corporation (SRC) program sponsored by DARPA. Part of this work was carried out in the Minnesota Nano Center, which was supported by the National Science Foundation through the National Nano Coordinated Infrastructure Network (NNCI) under Award No. ECCS-1542202. At CSU, the film growth was supported by the U.S. National Science Foundation (No. EFMA-1641989), and the film characterization was supported by the U.S. Department of Energy, Office of Science, Basic Energy Sciences (No. DE-SC0018994). We would also like to thank C-SPIN for the initial support of this project.

REFERENCES

- ¹A. Soumyanarayanan, N. Reyren, A. Fert, and C. Panagopoulos, Nature **539**, 509 (2016).
- ²A. Brataas, A. D. Kent, and H. Ohno, Nat. Mater. **11**, 372 (2012).
- ³O. Mosendz, J. E. Pearson, F. Y. Fradin, G. E. W. Bauer, S. D. Bader, and A. Hoffmann, Phys. Rev. Lett. **104**, 046601 (2010).
- ⁴K. Ando and E. Saitoh, J. Appl. Phys. **108**, 113925 (2010).
- ⁵K. Ando, S. Takahashi, J. Ieda, Y. Kajiwara, H. Nakayama, T. Yoshino, K. Harii, Y. Fujikawa, M. Matsuo, S. Maekawa, and E. Saitoh, J. Appl. Phys. 109, 103913 (2011).
- ⁶M. Jamali, A. Klemm, and J.-P. Wang, Appl. Phys. Lett. **103**, 252409 (2013).
- ⁷H. L. Wang, C. H. Du, Y. Pu, R. Adur, P. C. Hammel, and F. Y. Yang, Phys. Rev. Lett. **112**, 197201 (2014).
- ⁸J.-C. Rojas-Sánchez, N. Reyren, P. Laczkowski, W. Savero, J.-P. Attané, C. Deranlot, M. Jamet, J.-M. George, L. Vila, and H. Jaffrès, Phys. Rev. Lett. 112, 106602 (2014).
- ⁹V. M. Edelstein, Solid State Commun. 73, 233 (1990).
- ¹⁰Y. Shiomi, K. Nomura, Y. Kajiwara, K. Eto, M. Novak, K. Segawa, Y. Ando, and E. Saitoh, Phys. Rev. Lett. 113, 196601 (2014).
- ¹¹Y. Shiomi, K. T. Yamamoto, R. Nakanishi, T. Nakamura, S. Ichinokura, R. Akiyama, S. Hasegawa, and E. Saitoh, Appl. Phys. Lett. **113**, 052401 (2018)
- ¹²M. Jamali, J. S. Lee, J. S. Jeong, F. Mahfouzi, Y. Lv, Z. Zhao, B. K. Nikoli, K. A. Mkhoyan, N. Samarth, and J. P. Wang, Nano Lett. 15, 7126 (2015).
- ¹³H. Wang, J. Kally, J. S. Lee, T. Liu, H. Chang, D. R. Hickey, K. A. Mkhoyan, M. Wu, A. Richardella, and N. Samarth, Phys. Rev. Lett. 117, 076601 (2016).
- ¹⁴J. B. S. Mendes, O. A. Santos, J. Holanda, R. P. Loreto, C. I. L. De Araujo, C.-Z. Chang, J. S. Moodera, A. Azevedo, and S. M. Rezende, Phys. Rev. B 96, 180415(R) (2017).
- ¹⁵J.-C. Rojas-Sánchez, S. Oyarzún, Y. Fu, A. Marty, C. Vergnaud, S. Gambarelli, L. Vila, M. Jamet, Y. Ohtsubo, A. Taleb-Ibrahimi, P. Le Fèvre, F. Bertran, N. Reyren, J.-M. George, and A. Fert, Phys. Rev. Lett. 116, 096602 (2016).
- 16Z. Jiang, C.-Z. Chang, M. R. Masir, C. Tang, Y. Xu, J. S. Moodera, A. H. Macdonald, and J. Shi, Nat. Commun. 7, 11458 (2016).
- ¹⁷Q. Song, J. Mi, D. Zhao, T. Su, W. Yuan, W. Xing, Y. Chen, T. Wang, T. Wu, X. H. Chen, X. C. Xie, C. Zhang, J. Shi, and W. Han, Nat. Commun. 7, 13485 (2016)
- ¹⁸S. Zhang and A. Fert, Phys. Rev. B **94**, 184423 (2016).
- ¹⁹K. Shen, G. Vignale, and R. Raimondi, Phys. Rev. Lett. **112**, 096601 (2014).
- ²⁰J. C. Rojas Sánchez, L. Vila, G. Desfonds, S. Gambarelli, J. P. Attané, J. M. De Teresa, C. Magén, and A. Fert, Nat. Commun. 4, 2944 (2013).

- ²¹W. Zhang, M. B. Jungfleisch, W. Jiang, J. E. Pearson, and A. Hoffmann, J. Appl. Phys. 117, 17C727 (2015).
- ²²E. Lesne, Y. Fu, S. Oyarzun, J. C. Rojas-Sánchez, D. C. Vaz, H. Naganuma, G. Sicoli, J. Attané, M. Jamet, E. Jacquet, J. George, A. Barthélémy, H. Jaarès, A. Fert, M. Bibes, and L. Vila, Nat. Mater. 15, 1261 (2016).
- ²³S. Oyarzún, A. K. Nandy, F. Rortais, J.-C. Rojas-Sánchez, M.-T. Dau, P. Noël, P. Laczkowski, S. Pouget, H. Okuno, L. Vila, C. Vergnaud, C. Beigné, A. Marty, J.-P. Attané, S. Gambarelli, J.-M. George, H. Jaffrè, S. Blügel, and M. Jamet, Nat. Commun. 7, 13857 (2016).
- ²⁴S. Manipatruni, D. E. Nikonov, and I. A. Young, Nat. Phys. **14**, 338 (2018).
- ²⁵S. Manipatruni, D. Nikonov, C. Lin, tanay A. Gosavi, H. Liu, B. Prasad, Y. Huang, E. Bonturim, R. Ramesh, and I. A. Young, Nature 565, 35–42 (2018).
- ²⁶M. Matsushima, Y. Ando, S. Dushenko, R. Ohshima, R. Kumamoto, T. Shinjo, and M. Shiraishi, Appl. Phys. Lett. 110, 072404 (2017).
- ²⁷C. Hahn, G. De Loubens, O. Klein, M. Viret, V. V. Naletov, and J. Ben Youssef, Phys. Rev. B 87, 174417 (2013).
- ²⁸S. Emori, A. Matyushov, H.-M. Jeon, C. J. Babroski, T. Nan, A. M. Belkessam, J. G. Jones, M. E. Mcconney, G. J. Brown, B. M. Howe, and N. X. Sun, Appl. Phys. Lett. **112**, 182406 (2018).
- ²⁹M. Haertinger, C. H. Back, J. Lotze, M. Weiler, S. Geprägs, H. Huebl, S. T. B. Goennenwein, and G. Woltersdorf, Phys. Rev. B 92, 54437 (2015).
- ³⁰M. DC, R. Grassi, J.-Y. Chen, M. Jamali, D. R. Hickey, D. Zhang, Z. Zhao, H. Li, P. Quarterman, Y. Lv, M. Li, A. Manchon, K. A. Mkhoyan, T. Low, and J.-P. Wang, Nat. Mater. 17, 800 (2018).
- ³¹Y. T. Fanchiang, K. H. M. Chen, C. C. Tseng, C. C. Chen, C. K. Cheng, S. R. Yang, C. N. Wu, S. F. Lee, M. Hong, and J. Kwo, Nat. Commun. 9, 223 (2018).
- ³²X. Tao, Q. Liu, B. Miao, R. Yu, Z. Feng, L. Sun, B. You, J. Du, K. Chen, S. Zhang, L. Zhang, Z. Yuan, D. Wu, and H. Ding, Sci. Adv. 4, eaat1670 (2018).
- ³³Y. Tserkovnyak, A. Brataas, G. E. W. Bauer, and B. I. Halperin, Rev. Mod. Phys. 77, 1375 (2005).
- ³⁴H. Chang, P. A. P. Janantha, J. Ding, T. Liu, K. Cline, J. N. Gelfand, W. Li, M. C. Marconi, and M. Wu, Sci. Adv. 3, e1601614 (2017).
- 35 T. Liu, Y. Li, L. Gu, J. Ding, H. Chang, P. A. P. Janantha, B. Kalinikos, V. Novosad, A. Hoffmann, R. Wu, C. L. Chien, and M. Wu, Phys. Rev. Lett. 120, 207206 (2018).
- ³⁶M. Harder, Z. X. Cao, Y. S. Gui, X. L. Fan, and C.-M. Hu, Phys. Rev. B 84, 054423 (2011).
- ³⁷Q. Song, H. Zhang, T. Su, W. Yuan, Y. Chen, W. Xing, J. Shi, J. Sun, and W. Han, Sci. Adv. 3, e1602312 (2017).
- ³⁸P. Deorani, J. Son, K. Banerjee, N. Koirala, M. Brahlek, S. Oh, and H. Yang, Phys. Rev. B **90**, 094403 (2014).
- ³⁹A. J. Berger, E. R. J. Edwards, H. T. Nembach, A. D. Karenowska, M. Weiler, and T. J. Silva, Phys. Rev. B **97**, 094407 (2018).
- ⁴⁰K. Harii, T. An, Y. Kajiwara, K. Ando, H. Nakayama, T. Yoshino, and E. Saitoh, J. Appl. Phys. **109**, 116105 (2011).
- ⁴¹Y. Tserkovnyak, A. Brataas, and G. E. W. Bauer, Phys. Rev. Lett. 11, 117601 (2002).
- ⁴²M. Caminale, A. Ghosh, S. Auffret, U. Ebels, K. Ollefs, F. Wilhelm, A. Rogalev, and W. E. Bailey, Phys. Rev. B 94, 014414 (2016).
- ⁴³Y. Sun, H. Chang, M. Kabatek, Y.-Y. Song, Z. Wang, M. Jantz, W. Schneider, M. Wu, E. Montoya, B. Kardasz, B. Heinrich, S. G. E. Te Velthuis, H. Schultheiss, and A. Hoffmann, Phys. Rev. Lett. 111, 106601 (2013).
- ⁴⁴L. Liu, T. Moriyama, D. C. Ralph, and R. A. Buhrman, Phys. Rev. Lett. **106**, 036601 (2011).
- 45 K. Kondou, H. Tsai, H. Isshiki, and Y. Otani, APL Mater. 6, 101105 (2018).
- ⁴⁶M. Isasa, M. Carmen Martínez-Velarte, E. Villamor, C. Magén, L. Morellón, J. M. De Teresa, M. R. Ibarra, G. Vignale, E. V. Chulkov, E. E. Krasovskii, L. E. Hueso, and F.Casanova, Phys. Rev. B 93, 14420 (2016).
- ⁴⁷A. J. Berger, E. R. J. Edwards, H. T. Nembach, O. Karis, M. Weiler, and T. J. Silva, Phys. Rev. B 98, 024402 (2018).